Supporting Information for "An automatically updated S-wave model of the upper mantle and the depth extent of azimuthal anisotropy"

Eric Debayle[1], Fabien Dubuffet[1] and Stéphanie Durand[1]

Contents of this file

Introduction

———

Eric Debayle, Laboratoire de Géologie de Lyon : Terre, Planètes et Environnement. 2 rue Raphaël Dubois, Bâtiment Géode 69622 Villeurbanne Cedex, France. (Eric.Debayle@ens-lyon.fr)

[1]Laboratoire de Géologie de Lyon - Terre,

Planètes, Environnement, CNRS, UMR

5276, École Normale Supérieure de Lyon,

Université de Lyon, Université Claude

Bernard Lyon 1, 2 rue Raphaël Dubois,

Bâtiment Géode 69622 Villeurbanne Cedex,

France

This supporting information provides one table and 9 figures.

Table S1 summarizes the number of data used in our waveform modeling approach, as a function of period and mode number.

Figure S1 summarizes the stations and events coverage.

Figure S2 displays the output of a checkerboard test. The input model is a spherical harmonic of degree 20 and azimuthal order 8 (corresponding to a horizontal wavelength of ∼2000 km), with input perturbation of ± 5%. The input model is well recovered in the uppermost 200 km, although amplitudes are weaker in the central Pacific and beneath Africa. At 350 and 550 km depth, recovery is more strongly affected by data sampling and the input model is hardly recovered in Africa at 550 km depth.

In Figure S3, we try to recover a series of two input anomalies. Each couple of anomalies consists in two squares with 600 km sides and either +5% or -5% velocity perturbation. The two squares are distant by 600 km. In the uppermost 200 km of the mantle, we isolate the two input squares at most locations and recover about 50 % of their amplitudes. A slight tendency to merge anomalies is observed in some regions with weaker data sampling (Pacific ocean and southern Indian ocean). Amplitude recovery is a bit weaker at 350 and 550 km depth, and a tendency to merge anomalies is observed at the southernmost latitudes, especially beneath the Indian ocean and south America. The input anomalies at 550 km depth are well recovered beneath Africa, which was not the case in Figure S2. This illustrates how synthetic tests can be misleading, as they only show how a particular input model, which may or not have a component in the null space of the theory operator, is recovered [*Lévêque et al.*, 1993].

Figure S4 displays a comparison of our S-wave model, 3D2015_07Sv with two recent tomographic models, SL2013sv [*Schaeffer and Lebedev*, 2013] and SEMum2 [*French et al.*, 2013]. SL2013sv [*Schaeffer and Lebedev*, 2013] is obtained from an automated version [*Lebedev and van der Hilst*, 2008] of the Partitioned Waveform Inversion of *Nolet* [1990]. This approach is conceptually similar to the one used in this study and splits the construction of the tomographic model in two main steps. A non linear waveform inversion of individual seismograms yields path average constraints which are then combined in a tomographic inversion to obtain the 3D model. In both approaches, synthetic seismograms include fundamental and higher modes and are built using asymptotic and ray-based approaches.

SEMum2 [*French et al.*, 2013] uses a hybrid approach. Synthetic seismograms are generated in a 3D model using spectral-element forward modeling [*Komatitsch and Vilotte*, 1998]. To reduce computational costs, the crust is approximated by a smooth equivalent 3D model that matches global 25-60 s group velocity maps. Assuming that the smooth model accurately describes crustal effects in the period range of analysis, the obtained synthetics are "exact" in the sense that they account for all 3D effects generated by the initial model. Differences between synthetic and observed waveforms are then inverted using 2D kernels built using Nonlinear Asymptotic Coupling Theory (NACT, [*Li and Romanowicz*, 1995]). NACT kernels better represent the sensitivity of higher modes and long period body waves than path average kernels. SEMum2 therefore involves more sophisticated theories both in the forward and in the inversion modeling. The counterpart is the computational cost which imposes some limitations in the period range of analysis (only

periods ≥ 60 s are considered in SEMum2) and in the number of data (SEMum2 is based on 99,000 waveforms, against 750,000 in SL2013sv and up to 1,359,470 in 3D2015_07Sv). The idea of a model which includes most available data and which is updated in real time is therefore not applicable to SEMum2, as it would be computationally too expensive.

Figure S5 displays the spectra $S_A^2(l) = \sum_{m=-l}^{l} A_l^m A_l^{m*}$ of 3D2015_07Sv, SL2013Sv [*Schaeffer and Lebedev*, 2013] and SEMUM2 [*French et al.*, 2013].

Figure S6 shows correlations for spherical harmonic expansions of the models up to degrees 12, 35 and 60. Note that this kind of correlations are dominated by low spherical harmonic degrees which have largest spectral amplitudes. At degree 35, the observed correlations are similar to those found by *Chang et al.* [2015] for other recent seismic models.

Maps of SV-wave azimuthal anisotropy are shown at different depths in the upper mantle in Figure S7.

Figure S8 shows the anisotropy along the Absolute Plate Motion (APM). The dotted lines show the averaged anisotropy, which decreases with depth from about 2% at 100-150 km depths. The solid lines show the averaged anisotropy that is aligned with the absolute plate motion (APM) model NUVEL-1A [*DeMets et al.*, 1994] expressed in the no-net reference frame. This aligned anisotropy is very weak for plate velocities smaller than 3 cm yr^{-1}, increases significantly between 3 and 5 cm yr^{-1}, and saturates for plate velocities larger than 5 cm yr^{-1}. The maximum of aligned anisotropy is observed at 150 km depth for plates moving faster than 4 cm yr^{-1}. In *Debayle and Ricard* [2013], we show that for plates faster than 4 cm yr^{-1} , the alignment occurs at the full-plate scale.

Figure S9 displays Voronoi diagrams at different depths in the upper mantle. These diagrams are built using an approach described in *Debayle and Sambridge* [2004]. This approach guarantees that each cell of the obtained Voronoi diagram contains at least a seismic path in each 36° bin of azimuthal coverage. This requirement of at least 5 well distributed azimuths in each cell allows the determination of the anisotropy without aliasing effects. Voronoi diagrams provide a useful proxy for resolution. At each depth, the Voronoi diagrams are based on the ray coverage provided by our well resolved path averaged shear velocity models. We consider that the shear velocity is well resolved at a given depth when its a posteriori error is smaller than 80% of the a priori error *Debayle and Ricard* [2012]. A conservative choice is then to consider that azimuthal anisotropy is resolved when the size of the Voronoi cells is smaller than, or comparable to the correlation surface $2\pi L$, with L, the horizontal correlation length ($L = 200$ km in our case). Figure S9 shows that the quality criterion is satisfied on a uniform $2° \times 2°$ grid down to 450 km depth. At a depth of 650 km, the size of Voronoi cells increases principally at high latitudes in the southern hemisphere, in the eastern Atlantic and in western Africa. However, the size of the Voronoi cells remains everywhere smaller or comparable to the correlation surface, which ensures that there is enough azimuthal coverage to retrieve the SV-wave azimuthal variation everywhere in the upper mantle.

References

Chang, S.-J., A. M. G. Ferreira, J. Ritsema, H. J. van Heijst, and J. H. Woodhouse (2015), Joint inversion for global isotropic and radially anisotropic mantle structure including crustal thickness perturbations, *J. Geophys. Res.*, *120*(6), 4278–4300, doi:

10.1002/2014JB011824.

Debayle, E., and Y. Ricard (2012), A global shear velocity model of the upper mantle from fundamental and higher Rayleigh mode measurements, *J. Geophys. Res.*, *117*, doi:10.1029/2012JB009288.

Debayle, E., and Y. Ricard (2013), Seismic observations of large-scale deformation at the bottom of fast-moving plates, *EPSL*, *376*, 165–177, doi:10.1016/j.epsl.2013.06.025.

Debayle, E., and M. Sambridge (2004), Inversion of massive surface wave data sets: Model construction and resolution assessment, *J. Geophys. Res.*, *109*(B2), doi: 10.1029/2003JB002652.

DeMets, C., R. Gordon, D. Argus, and S. Stein (1994), Effect of recent revisions to the geomagnetic reversal time-scale on estimates of current plate motions, *Geophys. Res. Lett.*, *21*(20), 2191–2194, doi:10.1029/94GL02118.

French, S., V. Lekic, and B. Romanowicz (2013), Waveform Tomography Reveals Channeled Flow at the Base of the Oceanic Asthenosphere, *Science*, *342*(6155), 227–230, doi:10.1126/science.1241514.

Komatitsch, D., and J. Vilotte (1998), The spectral-element method: An efficient tool to simulate the seismic response of 2D and 3D geological structures, *Bull. Seismol. Soc. Am.*, *88*, 368–392.

Lebedev, S., and R. D. van der Hilst (2008), Global upper-mantle tomography with the automated multimode inversion of surface and S-wave forms, *Geophys. J. Int.*, *173*(2), 505–518, doi:10.1111/j.1365-246X.2008.03721.x.

Lévêque, J. J., L. Rivera, and G. Wittlinger (1993), On the use of checkerboard test to assess the resolution of tomographic inversions, *Geophys. J. Int.*, *115*, 313–318.

Li, X., and B. Romanowicz (1995), Comparison of global waveform inversions with and without considering cross-branch modal coupling, *Geophys. J. Int.*, *121*(3), 695–709, doi:10.1111/j.1365-246X.1995.tb06432.x.

Nolet, G. (1990), Partitioned waveform inversion and two dimensional structure under the network of autonomously recording seismographs, *J. Geophys. Res.*, *95*, 8499–8512.

Schaeffer, A. J., and S. Lebedev (2013), Global shear speed structure of the upper mantle and transition zone, *GJI*, *194*(1), 417–449, doi:10.1093/gji/ggt095.

Table S1. Number of selected data as a function of period and mode number (mode 0 for fundamental mode, mode X for the Xth overtone).

Period	mode 0	mode 1	mode 2	mode 3	mode 4	mode 5	Total/period
50	5,223,425	1,445,578	1,587,144	1,969,216	703,290	24,878	10,953,531
75	5,023,987	1,403,053	2,017,608	362,070	0	0	8,806,718
110	2,862,921	800,080	113,747	12	0	0	3,776,760
150	796,459	586,370	180,703	0	0	0	1,563,532
165	1,242,580	24,428	3,399	0	0	0	1,270,407
230	660,190	148,373	0	0	0	0	808,563
250	340,744	2176	0	0	0	0	342,920
350	462,172	12	0	0	0	0	462,184
Total/mode	16,612,478	4,410,070	3,902,601	2,331,298	703,290	24,878	27,984,615
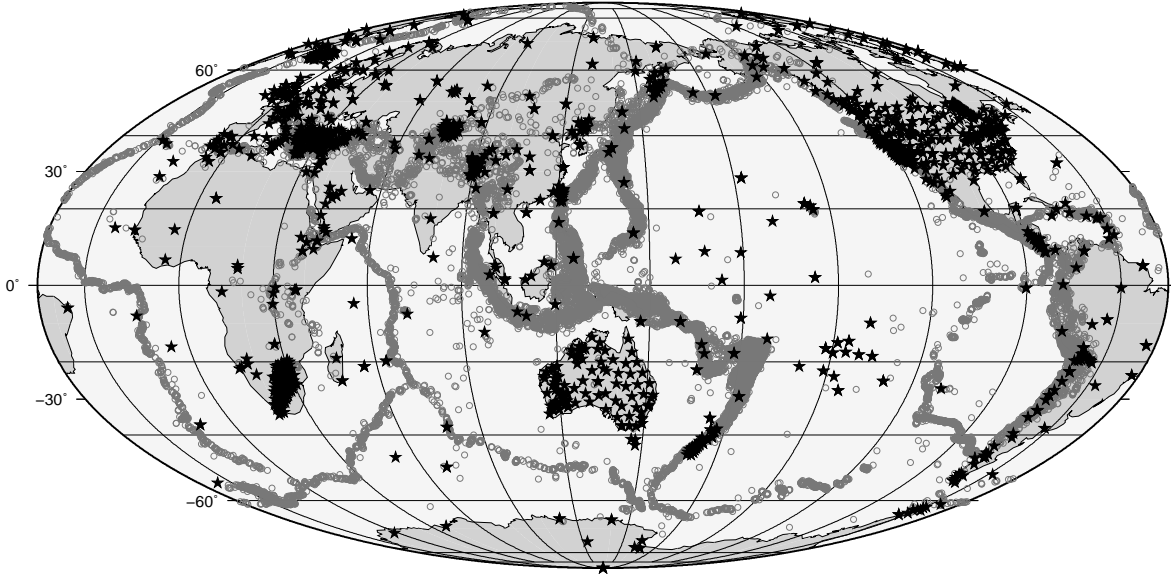
Figure S1. Location of the 30,469 events (circles) and 1,630 stations (stars) used in this study.
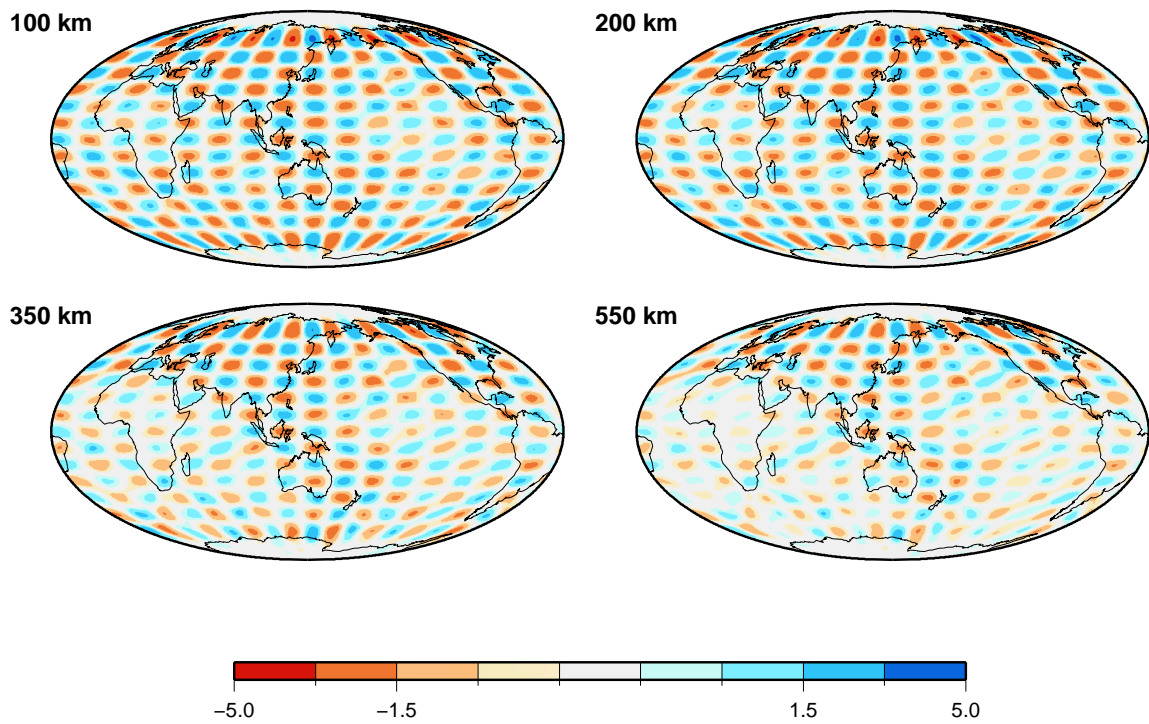
Figure S2.   Recovery of an input checkerboard model.
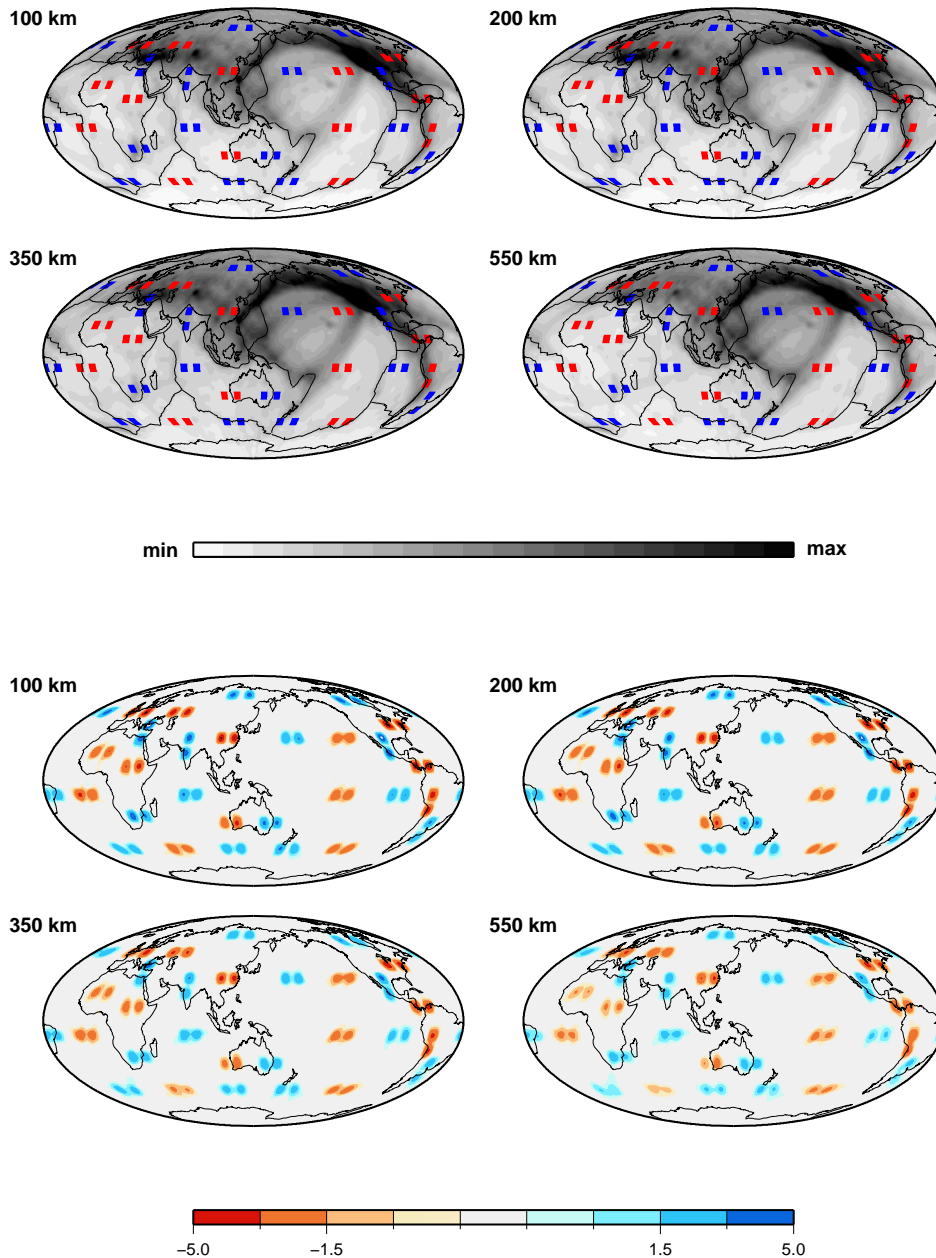
Figure S3.   Top : Input anomalies for a synthetic test (red and blue squares) superimposed to the relative lateral sampling at different depths. Input anomalies have sides of 600 km and either -5% (red) or +5% (blue) velocity perturbation. At each location, two input anomalies are placed and separated by a distance of 600 km. Relative sampling is estimated using column sum of the shear velocity parameter. The sampling is always greater than zero. Black and white scale is scaled to the min and max value for each depth. Bottom: Recovery of the input velocity model.
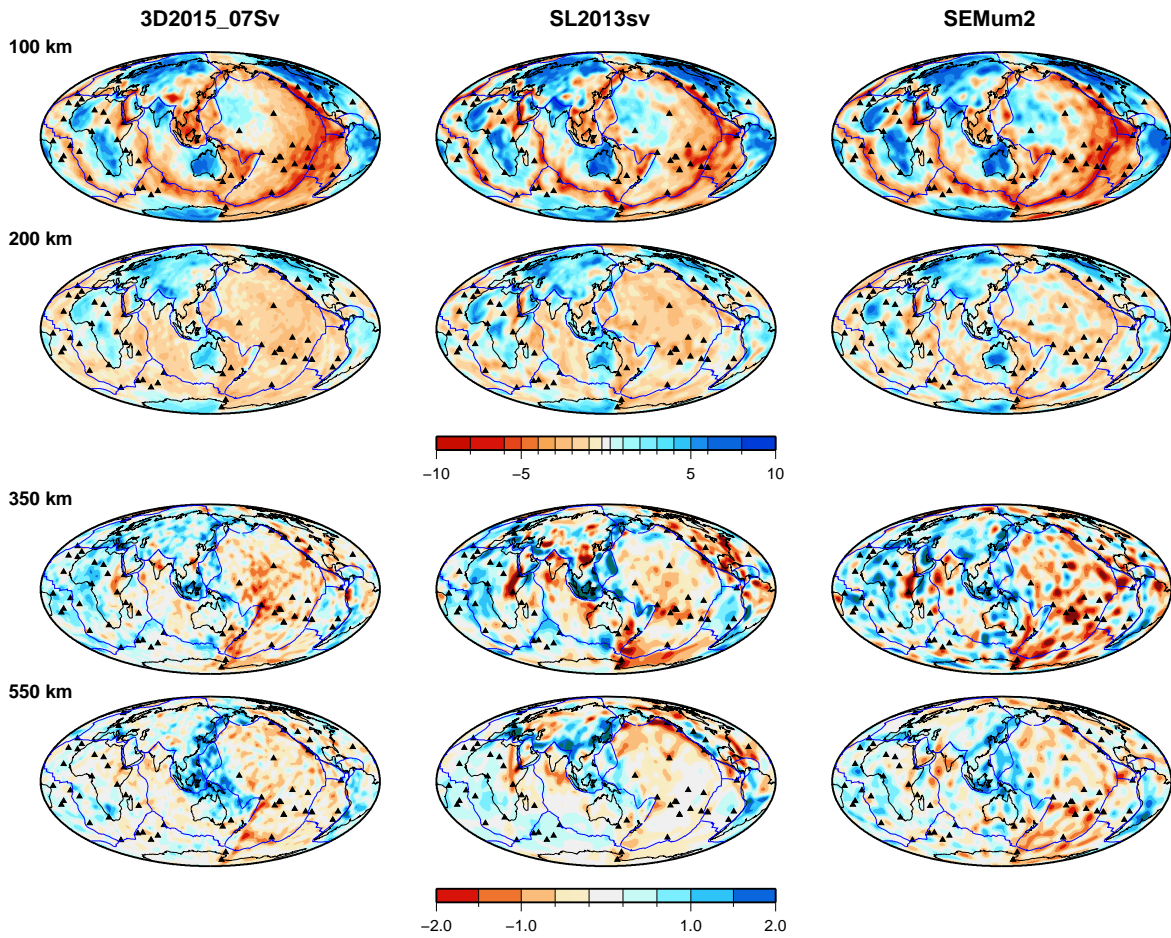
Figure S4.   Comparison of 3D2015_07Sv with two recent tomographic models : SL2013sv [*Schaeffer and Lebedev*, 2013] and SEMum2 [*French et al.*, 2013]. At each depth, perturbations are plotted in percent from the mean value for that model. The velocity varies from -10% to +10% from the average value in the uppermost 200 km. At greater depths, shear velocity perturbations are between -2% to +2% to emphasize smaller contrasts.
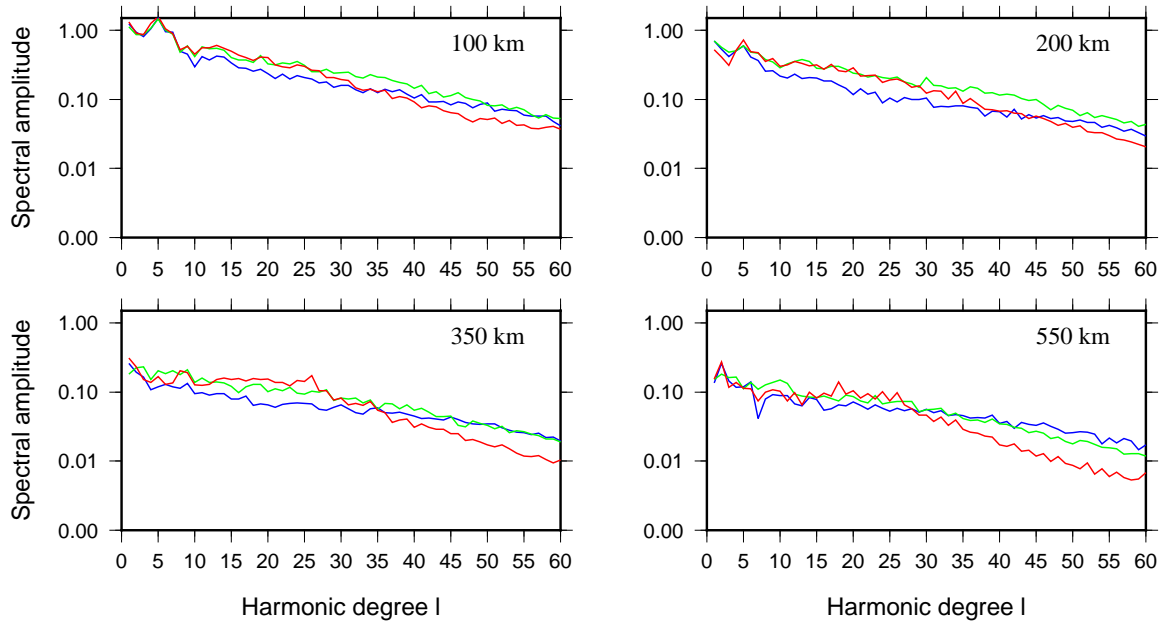
Figure S5.   Spectral amplitude as a function of spherical harmonic degree for 3D2015_07Sv (blue), SL2013Sv [*Schaeffer and Lebedev*, 2013] (green) and SEMUM2 [*French et al.*, 2013] (red).
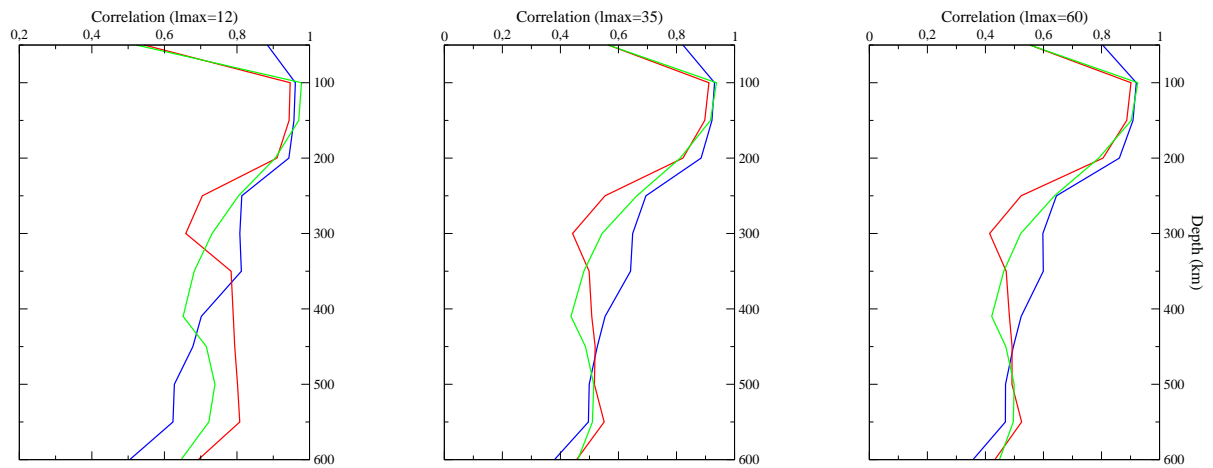
Figure S6. Correlation as a function of depth for spherical harmonic expansions of the models up to degrees 12, 35 and 60. Correlation between 3D2015_07Sv and SL2013sv [*Schaeffer and Lebedev*, 2013] (blue line); 3D2015_07Sv and SEMum2 [*French et al.*, 2013] (red line); SEMum2 [*French et al.*, 2013] and SL2013sv [*Schaeffer and Lebedev*, 2013] (green line).
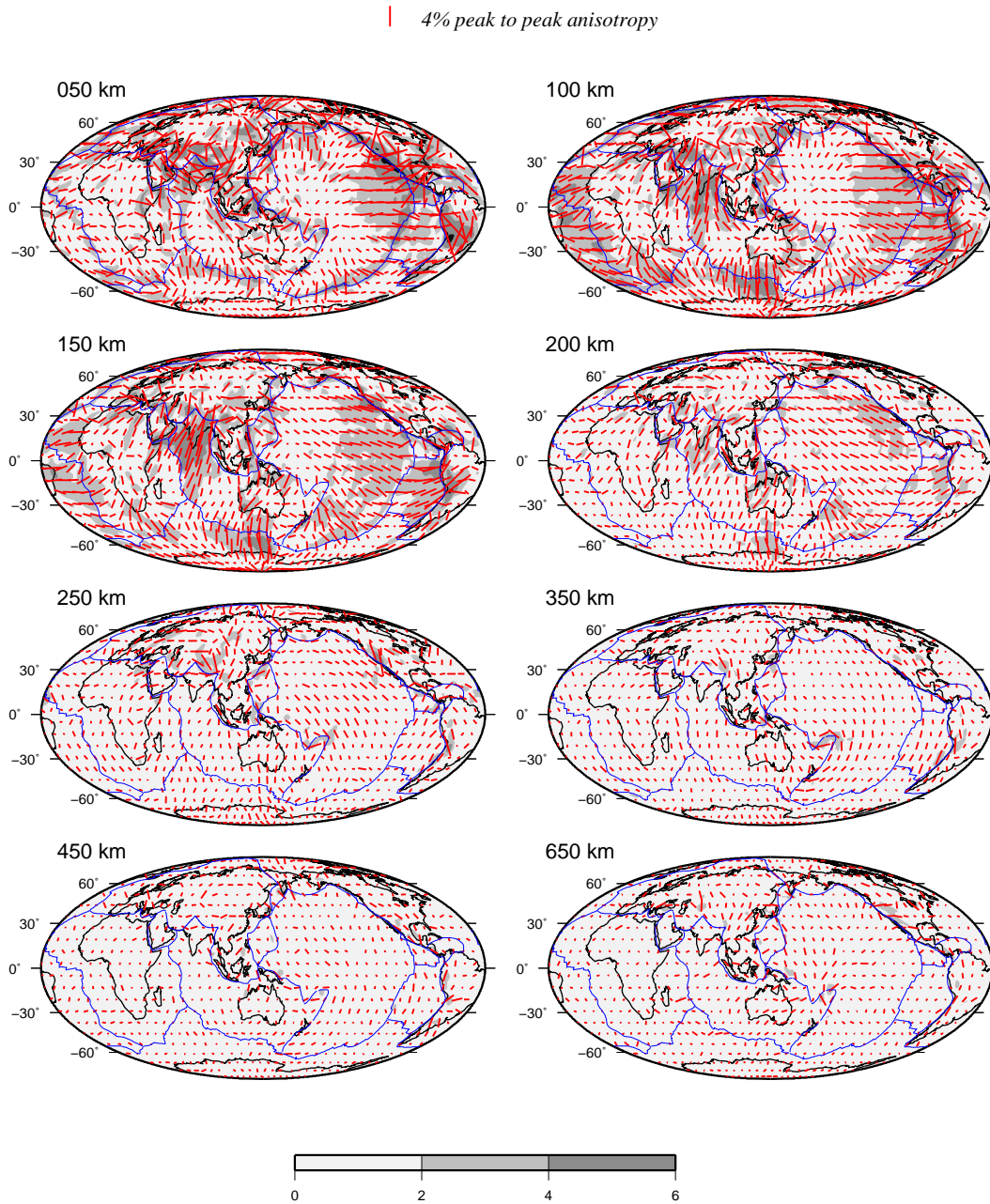
Figure S7. SV-wave azimuthal anisotropy (red bars oriented along the axis of fast propagation) at different depths in the upper mantle. The length of the bars is proportional to the peak to peak azimuthal anisotropy (bar length for 4% peak-to-peak anisotropy on top). The background gray scale indicates the amplitude of peak-to-peak azimuthal anisotropy in per cent.
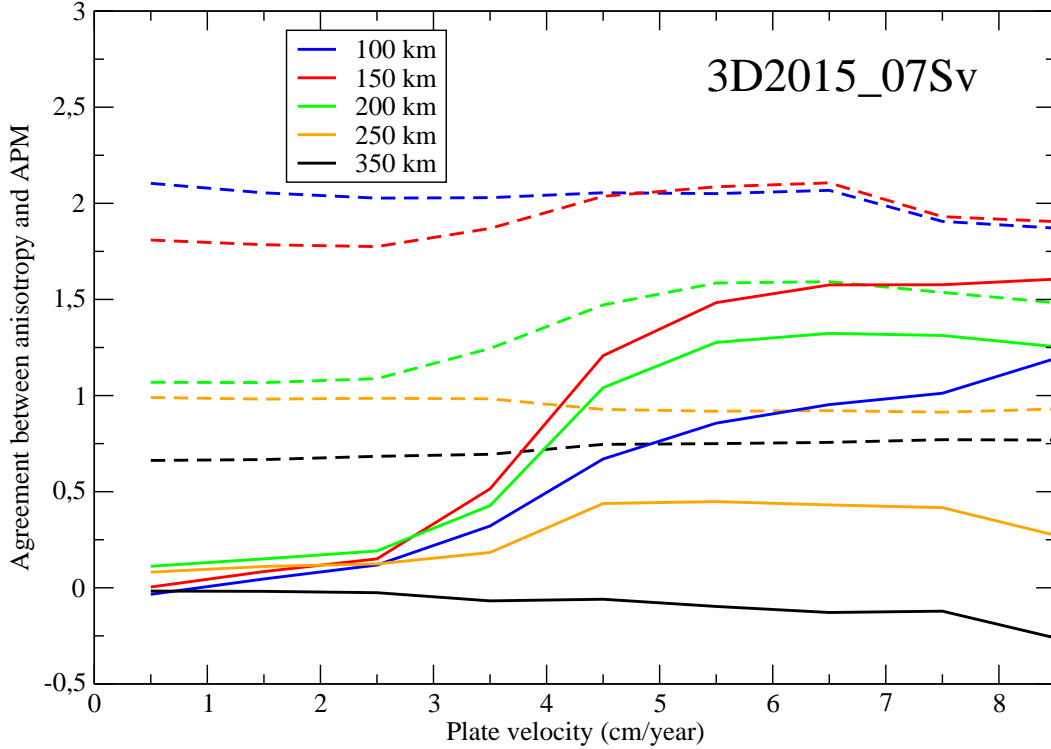
Figure S8.   The azimuthal anisotropy in 3D2015_07Sv is plotted along the APM, $<A\cos(2\alpha)>$ as a function of plate velocity (solid lines) for different depths in the upper mantle; A is peak to peak anisotropy in percent, α is the angle between APM and fast SV azimuth. $A\cos(2\alpha)$ is averaged for all geographical points with similar plate velocities, using a sliding window of ± 2 cm yr^{-1} width. Dotted lines show the peak to peak anisotropy strength $<A>$ as a function of plate velocities. Comparison of the dashed and continuous lines at a given depth indicates the maximum proportion of anisotropy which is parallel to APM.
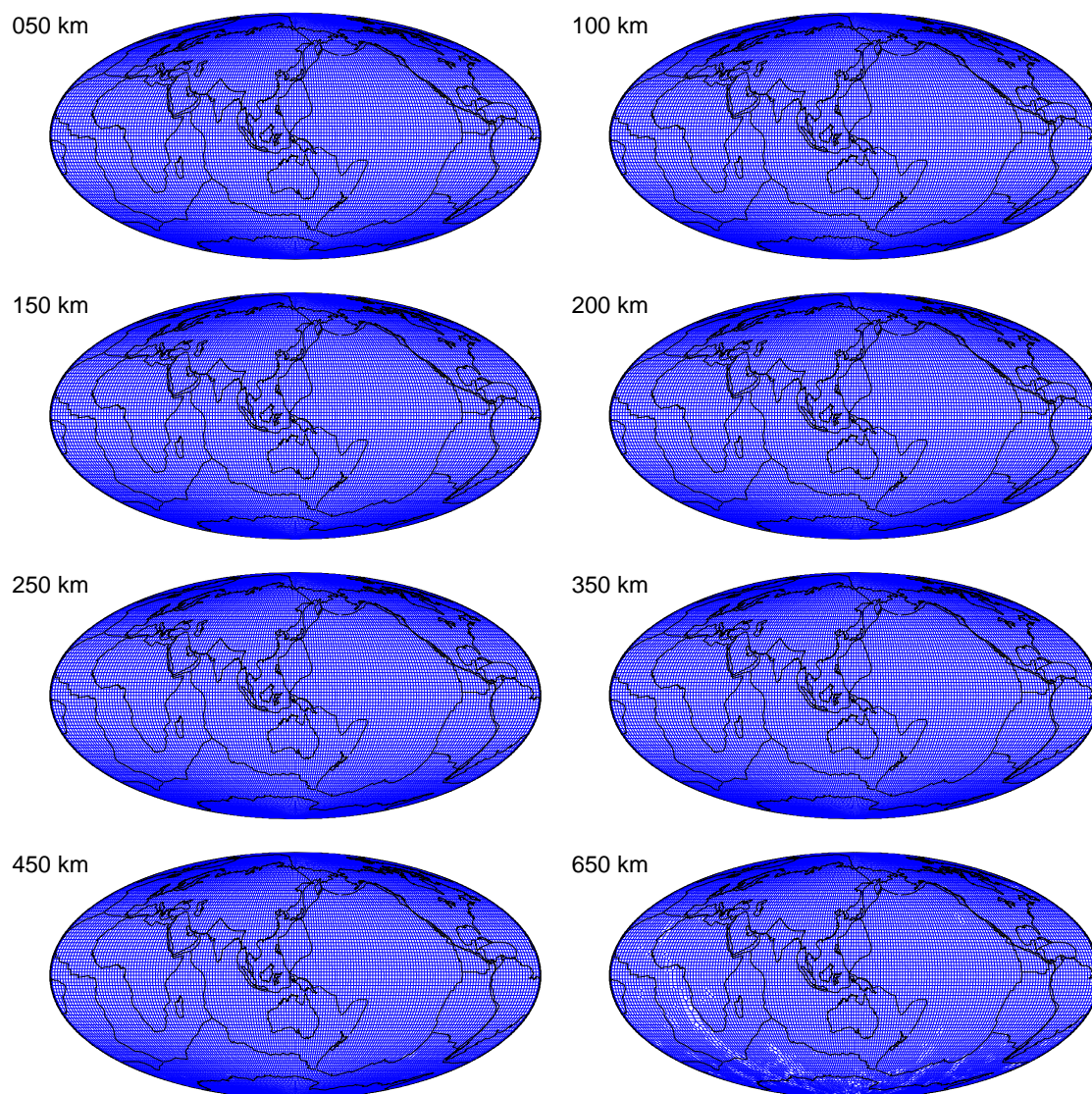
050 km

100 km

150 km

200 km

250 km

350 km

450 km

650 km

Figure S9.   Optimized Voronoi diagrams computed at different depths using the approach of

Debayle and Sambridge [2004]. Each cell of the diagrams shows the smallest region for which the

ray distribution allows resolution of the SV-wave azimuthal anisotropy.